Preprint Title	Morphological and force spectroscopy characterizations for indentification of surface nanobubbles from nanodroplets and blisters
Authors	Xiaolai Li, Binglin Zeng, Shuai Ren and Yuliang Wang
Publication Date	08 Mai 2020
Article Type	Full Research Paper
Supporting Information File 1	S1.pdf; 966.4 KB
ORCID® iDs	Yuliang Wang - https://orcid.org/0000-0001-6130-4321

Morphological and force spectroscopy characterizations for indentification of surface nanobubbles from nanodroplets and blisters

Xiaolai Li[1,2], Binglin Zeng[1,2], Shuai Ren[1] and Yuliang Wang[*1,3]

Address: [1]School of Mechanical Engineering and Automation, Beihang University, 37 Xueyuan Rd, Haidian District, Beijing, China; [2]Physics of Fluids, Max Planck Center Twente for Complex Fluid Dynamics and J.M. Burgers Centre for Fluid Mechanics, MESA+ Institute, University of Twente, P.O. Box 217, 7500AE Enschede, The Netherlands and [3]Beijing Advanced Innovation Center for Biomedical Engineering, Beihang University, 37 Xueyuan Rd, Haidian District, Beijing, China

Email: Yuliang Wang - wangyuliang@buaa.edu.cn

[*] Corresponding author

Abstract

Surface nanobubbles (NBs) play an important role in various practical applications, such as mineral flotation and separation, drag reduction, and nanostructured surface fabrication. Until now, it still remains as a challenge to identify surface NBs from other spherical-cap-liked nano-objects, like blisters and nanodroplets (NDs). Here we focus on the distinctions of NBs from NDs and blisters using an atomic force microscopy. It is implemented through morphological characterization, high load scanning, and force spectroscopy measurement. In the morphological characterization experiment, contact angles of the three types of nano-objects were compared. In the high load scanning experiment, the response of the nano-objects to high scanning loads was studied. The mobility, deformability, and volume change of the nano-objects during the high load scanning were investigated. At last, the force spectroscopy measurement was implemented. Due to the existence of the three-phase contact lines on both tip-NB and tip-ND interactions, force-distance curves ex-

hibit the similar behaviors on both NBs and NDs. However, quantitative analysis shows that the extracted parameters from force-distance curves can be used to distinguish one from the other. This study developed a systematic way to distinguish surface NBs from others nano-objects, which is crucial for surface nanobubble community.

Keywords

nanobubbles; blisters; nanodroplets; morphological characterization; force spectroscopy measurement; atomic force microscopy

Introduction

Surface nanobubbles (NBs) at solid liquid interfaces have attracted significant attentions in the last two decades because of their great potential in numerous applications, such as mineral flotation and separation [1], drag reduction [2-4], nanostructured surface fabrication [5-8] and the context of catalysis and electrolysis [9,10]. The properties of NBs have been investigated with numerous techniques, including atomic force microscopy (AFM) [11-13], x-ray reflectivity [14,15], infrared spectroscopy [16,17], and optical microscopy [18-20]. However, the NB community has long been suffering from the confusion caused by some other spherical cap shaped nano-objects, like nan-odroplets (NDs) [21,22] and blisters [23]. NDs may nucleate in NB experiments because of the im-purities in liquid. This is because NDs basically are similar to NBs regarding the nucleation mech-anism. The blisters are thin polymer film wrapped water pockets at solid-liquid interfaces on a thin film coated silicon substrate [24,25]. They are produced as water permeates through the thin film (i.e. a polystyrene film), wet and hence detach the thin films, leading to the formation of a water reservoir in between the supporting silicon substrate and the thin film [23,26]. So far it is still dif-ficult to distinguish NBs from these spherical cap shaped nano-objects, especially from NDs. NDs and NBs are all soft in nature, which makes it more challenging to distinguish one from the other with current imaging techniques.

Several research works have been performed to identify surface NBs [22,27-30]. The gaseous NBs

are expected to dissolve over time in degassed water. Thus the response of the nucleated spherical objects in degassed water was used to confirm the existence of surface nanobubbles [22,27]. The results show that NBs indeed could disappear in degassed water. However, Zhang *et al.* found that NBs can survive even after several hours of degassing [27]. This may be due to the cooperative shielding effects from neighboring NBs [28].

In Chan *et al.*'s study, they compared the interaction of retracting contact lines with NBs, NDs, and nanoparticles, the dynamic processes of which were recorded by a total internal reflection fluorescence (TIRF) microscopy [29]. Considerable different behaviors among NBs, NDs and nanoparticles were observed. Surface NBs rapidly collapsed while contacting with the retracting contact lines, while an accelerated receding and a pinning-depinning process were observed on the NDs and NPs, respectively. Meanwhile, Seo et al [30]. distinguished NBs from oil NDs covered by dyes with a fluorescence microscopy. The gas NBs and oil NDs absorb different fluorescent dyes, emitting fluorescence signals. All these methods provide evidence on the gas nature of NBs, with a limited spatial resolution though. However, the addition of dyes unavoidably alters the physcochemical properties of NBs or even causes their collapse, which is undesired in most of systems.

Recently, efforts were put on the distinction of surface NBs from other spherical cap liked objects by using AFMs, which guarantees high spatial resolution [31,32]. Wang *et al* produced polydimethylsiloxane (PDMS) NDs on highly oriented pyrolytic graphite (HOPG) [32]. By comparing their properties with that of NBs using an AFM, they found that PDMS NDs were very close to NBs in size, contact angle, and stiffness, but different from force-distance curves. They claimed that there was a plateau in the approach force distance curves acquired on NBs, but not on the PDMS NDs. In the tip-nanodroplet interaction process, a linear force-depth curve was observed.

An *et al.* also identified NBs from PDMS NDs with an AFM [31]. Their results show that NBs and NDs exhibit distinct responses under higher vertical and lateral forces. In PeakForce mode, they found that NBs are invisible in AFM height images under large vertical imaging forces in the order of tens of nN, but NDs maintain a nanometric molecular layer. They also found that NBs are strongly pinned on substrates and survive large lateral imaging forces of up to 50 nN without being

moved or destroyed in the contact mode AFM. NDs are weakly pinned and can be easily moved. However, in Wang *et al.*'s work, they observed a linear dependence of AFM cantilever deflection, which is proportional to force, on the penetration depth of AFM tips into NBs. While the interaction curve on nanodroplet shows sharp kinks. This is in conflict with what was reported in An's work.

In this work, the spontaneous formation of NBs on a hydrophobic surface was adopted to avoid addition of any other solvent and then minimize the chance of contamination. By employing nano-manipulation and force spectroscopy measurement of AFM tips on NBs, NDs, and blisters, a systematic investigation was conducted to distinguish NBs from NDs and blisters. We find that NBs are distinguishable from three aspects: (a) volume changes before and after coalescence, (b) response to higher loads, and (c) force spectroscopy measurement.

Experimental section

(i) Sample preparasion

The polystyrene (PS) surfaces used for NB and blister nucleation were prepared by spin coating thin films of PS on silicon (100) substrates at a speed of 1000 rpm. Before spin coating, the substrates were sequentially cleaned in sonication bathes of piranha, acetone, and then water, each for 30 min. PS particles (molecular weight 350 000, Sigma-Aldrich) were dissolved in toluene (Mallinckrodt Chemical) to make the PS solutions. Two PS films, PS sample 1 and PS sample 2, were prepared. The PS concentrations for sample 1 and sample 2 are 1.0% and 0.5%, respectively. The lower PS concentrations leads to a thinner PS film and may cause surface defects [33], which are necessary for blister formation [23].

A HOPG (10×10 mm^2, ZYH grade, SHNTI, Shanghai, China) surface was freshly cleaved as the substrate for PDMS ND nucleation. A PDMS solution with a concentration of 1/2000 (v/v) was prepared by dissolving 0.1 mL PDMS (Sylgard 184, Dow Corning, United States) into 200 mL chloroform.

(ii) Nucleation of NBs, NDs and blisters.

Generally speaking, there are two approaches to produce NBs [34]. One is the spontaneous nucleation by simply depositing water on hydrophobic surfaces. Surface nanocavities trap air pockets and lead to the nucleation of NBs [11]. The other is achieved by solubility adjustment. By exchanging solvent or producing temperature differences, local gas supersaturation can be achieved, resulting in the nucleation of NBs. In this study, the spontaneous nucleation of NBs was adopted. The water was first kept in air for more than 10 hours for air diffusion. To avoid the possible contamination originating from the disposable needles of plastic syringes [22,35], a glass syringe was used to add water on the PS surface. Moreover, degassing experiments were conducted to verify the gaseous nature of the generated nanobubbles. For detailed results, please refer to SI. Blisters were formed by immersing PS sample 2 into DI water.

The chloroform-PDMS mixture was applied to produce PDMS NDs with controllable sizes. Since the chloroform can dissolve PS substrates, here NDs were nucleated on a HOPG substrate. First, 20 microliter PDMS-chloroform solution was deposited onto the freshly cleaved HOPG substrate. After the rapid volatilization of chloroform, the substrate with remained PDMS was immersed in water by depositing a water drop (200 microliter). The PDMS NDs was then nucleated at the water/HOPG interface.

(iii) AFM Characterization.

A commercial AFM (Resolve, Bruker, U.S.A.) was used for imaging the sample in both air and DI water. Silicon cantilevers (NSC36/ALBS, MikroMasch) with the quoted tip radius of 8 nm and stiffness of 0.6 N/m from the manufacturer was used. The measured resonance frequencies of the cantilever in air and water were about 55 kHz and 16 kHz, respectively. While imaging, the driving frequencies of cantilevers were slightly lower than their resonance frequencies. A scan rate of 2 Hz with a 0° scan angle was used. All experiments were performed at an ambient environment (temperature: 26 °C).

5

All sample surfaces were first scanned in air by the tapping mode AFM (TMAFM). After that, the imaging was performed in liquid. The cantilever's spring constant for scanning NBs, NDs and blisters are 3.2, 2.8 and 3.1 N/m, respectively, which were calibrated by a thermal noise method. The free oscillation amplitude of the cantilever at working frequency was about 200 mV. During experiments, the nucleated NBs, NDs and blisters were first scanned with a larger oscillation amplitude setpoint of about 195 mV (namely 98% of free amplitude) to minimize the disturbance of AFM tips to sample surfaces. To investigate the mobility of the three objects, higher scanning loads were used. After that, 98% setpoint scanning was performed again to check the consequence of high load scanning. The scan areas for NBs and NDs are 2 μm$\times$ 2 μm, and 5 μm$\times$ 5 μm for blisters. Subsequently, smaller areas (around 600 nm$\times$ 600 nm) with individual NBs, NDs and blisters were selected to perform a successive scans with setpoint values varying from 98% to 60%.

Force volume mode AFM was used to get several series of force-distance curves on a NB, a ND, and a blister. In the mode, the AFM cantilevers perform force-distance curve measurement in a specific area with fixed step sizes along x and y axes. At each scan position, the AFM scanner performs a vertical extension and retraction motion relative to the sample surface under constant driving frequency and amplitude, and a force distance curve was then obtained. The ramp size for the extension and retraction motion was 200 nm and the scan rate was 1 Hz. The step sizes along both x and y axes for NBs and NDs experiments were 20 nm, within a scan area of 500 nm$\times$ 500 nm. The AFM images are processed with a home designed algorithm for image segmentation, contact angle measurement and volume calculation [36-39]. All calculations were performed in MATLAB 2016.

Results and Discussion

Morphological characterization and high load scanning

The images of PS surface 1, HOPG, and PS surface 2 in air are shown in Figure 1 (a), (b) and (c), respectively. All these surfaces are smooth in air. Corresponding AFM images of NBs, NDs and

6

blisters in deionized (DI) water were depicted in Figure 1 (d), (e) and (f), respectively. To minimize the influence of the high load scanning on the measured morphology, these images were captured under a very low scanning load with a setpoint of 98% of free amplitude of the AFM cantilevers. One can see that NBs and NDs have relatively uniform distribution of lateral size L, while L varies a lot for blisters.
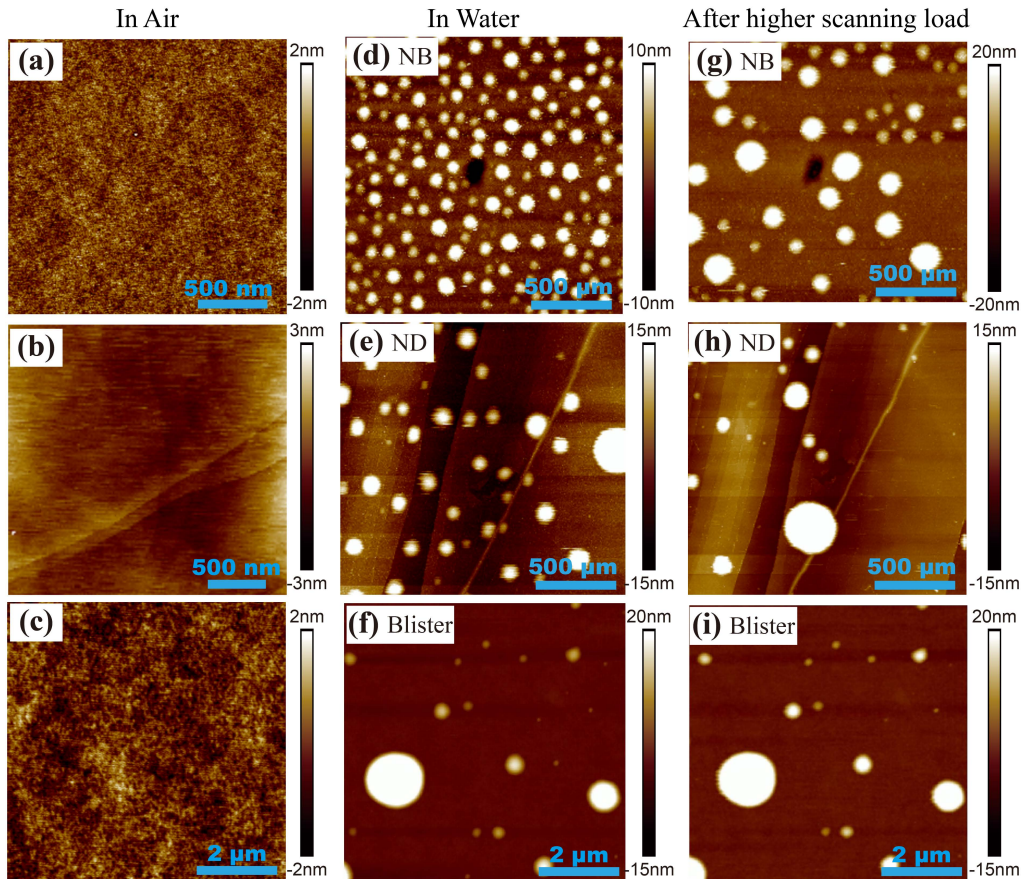
Figure 1: Generation of NBs, NDs, and blisters and their response to high scanning loads. (a)-(c) The PS surface 1 (a), HOPG surface (b), and PS surface 2 (c) in air. (d)-(f) The generated NBs (d), NDs (e), and blisters (f) after the surfaces were immersed in water. (g)-(i) AFM images of the NBs, NDs, and blisters after high load scans. The NBs and NDs are movable and larger NBs and NDs formed after coalescence. The blisters remain at the same positions regardless of the scanning load.

AFM images also reveal that the three objects exhibit different aspect ratios. Figure 2 depicts the contact angle θ of NBs, NDs, and blisters from the gas, oil, and solid side, respectively. It clearly shows that θ increases with L for both NBs and NDs. On the contrary, θ is independent of L for

blisters. In addition, NBs and NDs have larger θ than that of blisters, and θ for NBs is slightly lower than ND.

The response of NBs to higher load scanning is a typical approach to study their physical properties [31,38]. Here a higher scanning load (setpoint 60%) was applied for imaging. After that, a 98% setpoint lower load scanning was applied to the same areas to observe the change of sample surfaces. The results are shown in Figure 1 (g-i). It shows that the NBs and NDs were moved and coalesced during the higher load scanning. As a result, larger NBs and NDs were nucleated (Figure 1g and h). However, no apparent change was observed for blisters. They all remained at the same positions after the high load scanning.
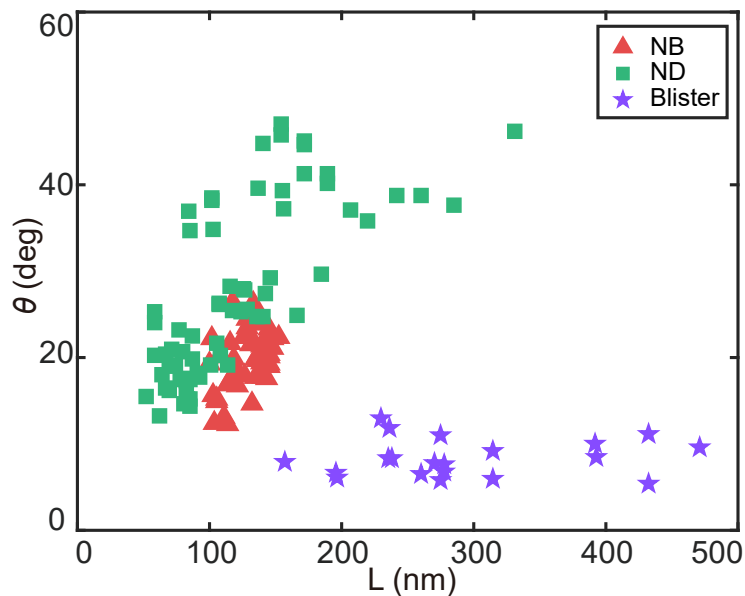
Figure 2: Contact angles of NBs, NDs and blisters as a function of diameter. The contact angles of NBs and NDs increase with increasing lateral size, and are larger than that of blisters. The contact angle of blisters is independent of their diameter.

The observed coalescence of NBs is consistent with that reported somewhere else [11]. Under a higher scanning load, larger lateral force can be applied to nano-objects. For NBs, when the lateral force exceeds the pinning force origin at the solid-liquid-gas three-phase contact lines, they can be moved and hence coalesced with neighboring ones. This leads to formation of larger NBs with reduced area density. The mechanism has been well studied in our previous studies. A term *immobility* was proposed to associate surface nanostructures to the resistance of NBs to lateral forces [40].

8

NDs share the same mechanism of movement and coalescence under the higher scanning loads [22]. An *et al.* reported that moving NDs is even easier than that of NBs [31]. While for blisters, they are actually PS film wrapped water pockets [23]. They cannot be moved with a tapping mode AFM, not to mentioned the following coalescence.

The above results show that NBs and NDs exhibit distinct behaviors from blisters under higher scanning loads. Therefore, one can easily distinguish blisters from NBs and NDs. The difference between NBs and NDs under the high scanning loads worths further investigation. Here the volume of NBs and NDs before and after coalescence were compared with a home-designed algorithm (refer to SI for details). Interestingly, we find that the volume change before and after the coalescence is quite different between NBs and NDs, as shown in Table 1. The total volumes V_{nb} and V_{nd} before coalescence in Figure 1 (d) and (e) are 4.55×10^6 nm^3 and 1.05×10^7 nm^3 for NBs and NDs, respectively. After coalescence (Figure 1 g and h), the total volumes are $V_{nb}=1.1 \times 10^7$ nm^3 and $V_{nd}=1.11 \times 10^7$ nm^3 for NBs and NDs, respectively.

Table 1: Volume change of NBs and NDs before and after coalescence.

	Before coalescence	After coalescence
V_{nb} ($\times 10^6 nm^3$)	4.55±0.29	11.00±0.20
V_{nd} ($\times 10^7 nm^3$)	1.05±0.03	1.11±0.02

The increment of NB volume is highly repeatable among different experiments (see the repeated experiment in SI). We believe that this is because of the reduced inner pressure with increasing NB size. According to Young-Laplace equation,

$$p_g = p_0 + \frac{2\gamma_L}{R}, \tag{1}$$

where p_0 is the ambient pressure, γ_L is surface tension of water, and R is the radius of NBs. Assuming that the NBs are equilibrated with each other and the gas concentration in the edge of bubbles is constant, the inner pressure p_g rapidly reduces with increasing R. This has two con-

sequences. First, based on the ideal gas law, the gas molecules originally trapped in NBs before coalescence will occupy more space when p_g is reduced. This leads to increased bubble volumes. Moreover, the reduced inner pressure p_g enhances the diffusion of the dissolved gas in water into NBs. This further increases NB volume. Regarding the NDs, as expected, the volumes are almost the same before and after the coalescence. The results indicate that the content in the spherical objects on PS surface 1 are indeed gas.

After the 60% setpoint high load scanning, the successive AFM scans with setpoints from 98% to 60% of the free oscillation amplitude were conducted. The morphology of NBs and NDs changed significantly with decreasing setpoints, *i. e.* imaging forces, as shown in figure 3(a) and (b). The cross section profiles of NB and ND height images decreases with increasing scanning forces. The cross section profiles obtained with setpoints larger that 80% still exhibit circular arc shape. Notably, the NB become almost flat at the lowest setpoint of 65%, while the ND appeared as a sombrero (a spherical cap sitting on a flat molecular layer) at setpoints of 70% and 60%. Comparing with the NB, the ND has larger resistance to vertical loads and can still maintain its circular arc shape for setpoints down to 60%. This is because the gaseous NBs are softer than NDs, thus easier to be deformed by AFM tips [31,34,41]. Particularly, the remained molecular layer of ND under larger vertical loads have been observed in several previous studies [31,42], which is consistent with our results, although the underlying mechanism is till not well understood. Unsurprisingly, the height of blister in figure3 (c) only slightly decreases in height with increasing scanning forces, exhibiting a solid-like response to scanning loads.

Force spectroscopy

To distinguish one from the other in between NBs and NDs, the force spectroscopy characterization was conducted through tip-sample interaction measurement using the AFM. By tracking the vertical deflection signal of a AFM cantilever as it approaches and retracts from sample surfaces, the mechanical signatures of the three objects were revealed.

Figure 4 (a)-(c) depict three typical force-distance curves on a NB, a ND, and a blister, respectively.

10
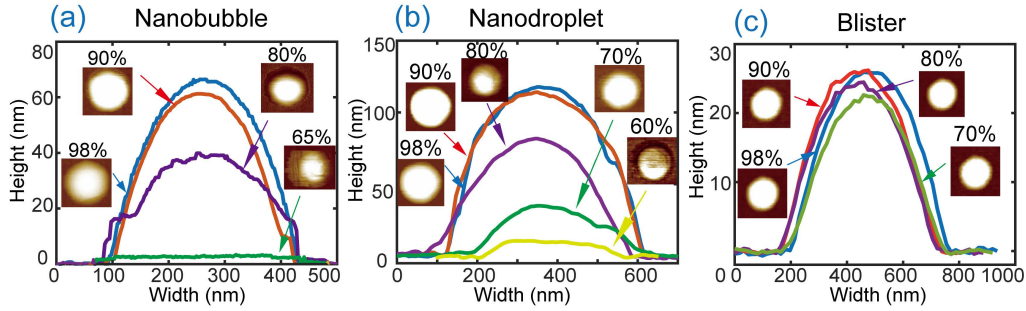
Figure 3: Morphology change of the three different surface nano-objects under various scanning loads. The cross section profiles of a NB (a), a ND (b) and a blister (c) with increasing scanning loads of setpoints from 98% to 60%. The height profiles of the NB and ND both reduce with the increasing imaging force, while the height for the blister does not change much.

The insets are corresponding AFM height images of the three nano-objects. Here a NB and a ND with a similar footprint diameter were produced through coalescence to minimize the influence of their sizes on the characterization. Figure 4(d) and (e) are schematics of the different stages of tip-NB/ND and tip-blister interaction, respectively. Note here that the downward motion direction of the z piezo stage is defined as the positive direction.

As shown in section 1 of figure 4 (a), when the tip is far away from the substrate (in liquid), there is no interaction between them and thus the deflection remains constant at zero (figure 4 (d)-1). Once the AFM tip contacts the NB, the tip is rapidly drawn into the NB due to the capillary force (figure 4 (d)-2). Therefore, an obvious snap-in is observed in section 2. This is consistent with the previous studies [40,43-45]. In section 3, the deflection linearly increases with piezo vertical position Z. That is because that the perimeter of the three-phase contact line increases with insertion depth of the cantilever tip into the NB. As a result, the force applied to the tip from the three-phase contact line also show linear dependence on z, as illustrated in figure 4(d)-3.

When the tip further goes down, it touches the solid sample surface (figure 4 (d)-4). This hard contact results in a rapid linear increase of cantilever deflection with increasing piezo vertical position z in section 4. After the AFM z scanner goes to the minimum vertical position, it reverses its motion and starts the retraction motion. It starts from the rapid linear decrease of the deflection signal. After that, it enters the linear reduction part (section 5, figure 4 (d)-5), until the tip snaps out of the NB (section 6, figure 4 (d)-6). Finally, the deflection become zero in section 7 (figure 4 (d)-7).

11
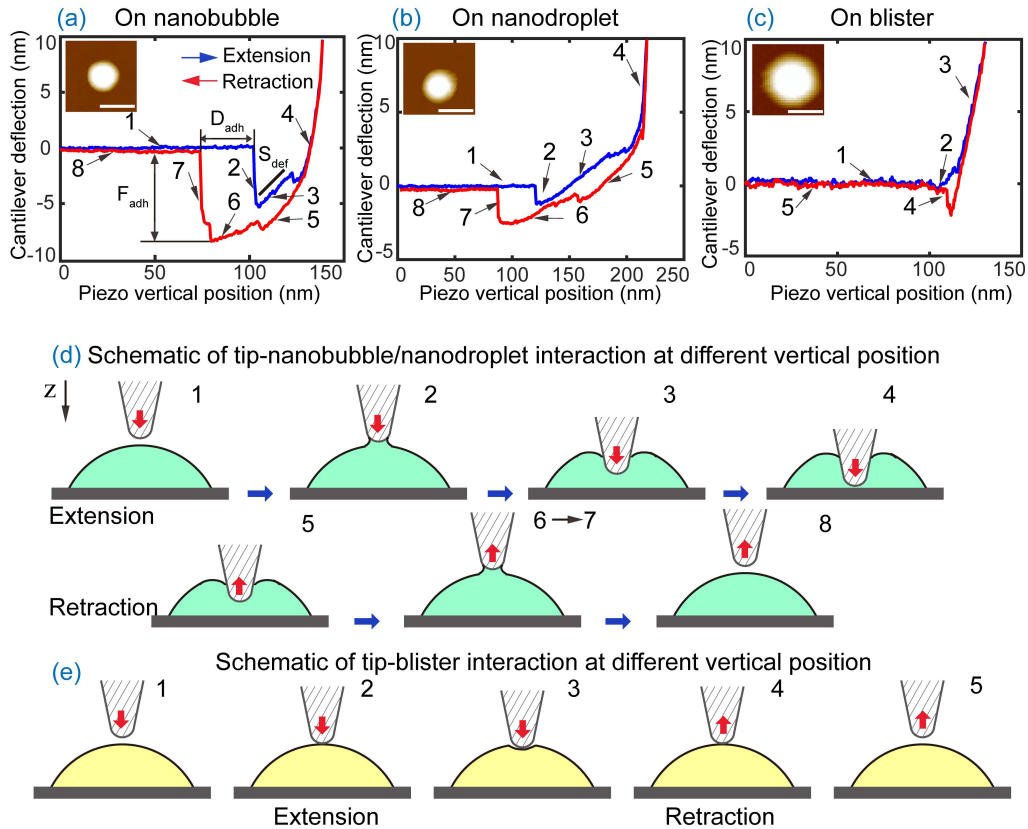
Figure 4: Force spectroscopy measurement through force-distance curves. (a-c) Typical force-distance curves obtained on a NB (a), a ND (b) and a blister (c). (d) The schematic of tip-NB/ND interaction. The numbers 1-8 correspond to the different stages labeled on the force distance curves in (a) and (b). (e) The schematic of tip-blister interaction, indicating the five stages along with the force curve.

Notably, the AFM tip used here is silicon, which is hydrophilic. Previous studies demonstrate that the hydrophobicity of AFM tips can significantly influence tip-bubble interactions and hence the bubble imaging [46,47]. For hydrophobic tips the bubble interface may jump towards the tips. This results in a large snap-in of the force curves and cause larger bubble deformation. In contrast, scanning with a hydrophilic tip provides reliable tip-bubble interaction curves as well as less distorted bubble images. In addition, the linearity of the tip-bubble interaction region also depends on the hydrophobicity of the tips [45]. With a hydrophilic tip, the tip-bubble interaction shows better linearity and exhibits a lower slope value.

The tip-ND interaction is very similar to the tip-NB interaction (figure 4 (b)). However, tip-blister

interaction exhibits distinct behaviors from that of tip-NB/ND interactions, as shown in figure 4 (c). The force curves measured on the blisters is close to that measured on the bare PS substrate. The schematics in figure 4 (e) illustrate the different stages of tip-blister interaction in figure 4 (c). One can see that blisters more behave as solid objects in tip-sample interaction measurement.

With the above force spectroscopy measurement, it is easy to distinguish NBs from blisters. However, force-distance curves on the soft objects of NBs and NDs are very close to each other. In order to further investigate the difference between NBs and NDs, we extract several key indicators from force distance curves.

As shown in Figure 4 (a), the prefactor S_{def} in the linear interaction region of section 3, the maximum adhesion force F_{adh} and the distance D_{adh} can be obtained for individual force distance curves. By performing the force volume mode measurement, a series of force-distance curves at specific positions of NBs/NDs were acquired. For each force-distance curve, the three parameters were manually extracted. The prefactor S_{def} in section 3 is the derivative of vertical forces to vertical piezo distance z. According to Ref [45], $S_{def} \propto \gamma_L$, where γ_L is the liquid/gas surface tension of water. Thus the prefactor S_{def} indicates the surface tension of the object which the tip penetrates into. The surface tension of water/air and water/PDMS interfaces are 72 mNm^{-1} and 40 mNm^{-1}, respectively. Figure 5 (a) and (b) are the constructed maps of S_{def} on NBs and NDs, respectively. Figure 5 (c) shows the histograms of S_{def} on the NB and the ND. One can see that S_{def} on the NB is much larger than that on the ND, which is consistent with the derived mathematic model in Ref [45].

The value F_{adh} is the adhesion force between the AFM tip and the NB/ND at the moment of snap-out. Since the radius of the NB is about 1000 times larger than that of the AFM tip, the NB can be approximated as a planar surface when modeling the tip-NB interaction. By assuming that the tip was in contact with a continuous film, the attractive force F_{adh} due to the meniscus bridge for a sphere in contact with a plane surface can be expressed as [45]

$$F_{adh} = 2\pi R \gamma_L (1 + cos\theta), \tag{2}$$

13
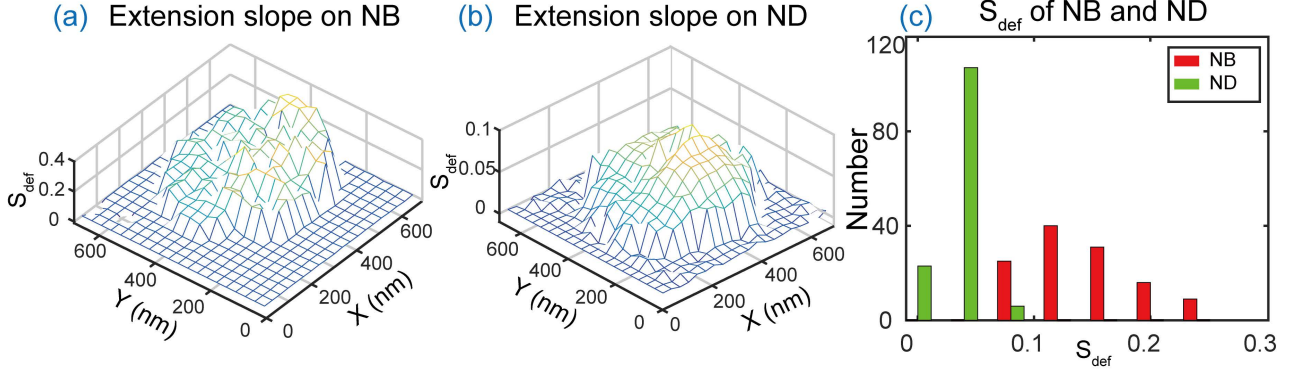
Figure 5: Comparison of the prefactor S_{def} in the linear interaction region of force-distance curves between a NB and a ND. The constructed maps of S_{def} for the NB (a) and the ND (b). (c) The histograms of S_{def} on the NB and the ND. The NB exhibits much larger value of S_{def}.

where R is the radius of the sphere (tip radius here), γ_L is the water/gas (NB case) or water/PDMS (ND case) surface tension, and θ is the contact angle of AFM cantilever on the NB or ND. The constructed maps of F_{adh} on the NB and the ND are shown in Figure 6 (a) and (b), respectively. We find that the NB have much higher value of F_{adh} comparing to the ND. This is consistent with the reported surface tension values at the three phase contact lines of the NB and ND.
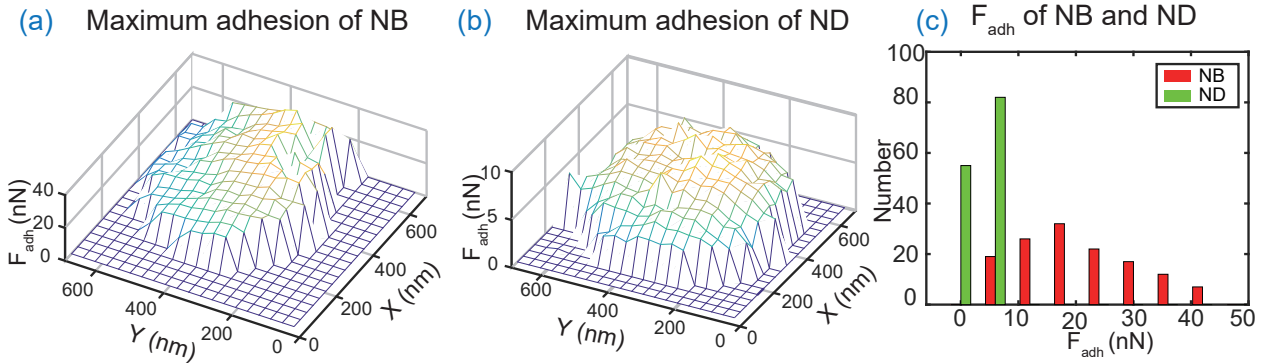
Figure 6: Comparison of the tip-sample adhesion force between the NB and the ND. The constructed maps of the adhesion force F_{adh} for the NB (a) and the ND (b). (c) The histograms of the adhesion force F_{adh} on the NB and the ND. The NB has much larger F_{adh}.

The parameter D_{adh} extracted from the force distance curves is the length of pulled capillary bridge, namely, the deformation of the NB/ND when the tip detaches from them. In most cases, the capillary bridge can be pulled out for a limited distance before the AFM tip eventually detaches.

14

As shown in Figure 7, the D_{adh} of the NB is smaller than that of the ND. This result indicates that the ND has a much larger capillary bridge than that of the NB. The medium value of D_{adh} on the ND is about 36 nm, which is about three times of the value measured on the NB. This is because that the droplet of PDMS is non-Newtonian liquid. That can stretch longer, since the stretching modifies the stress balance anisotropically.
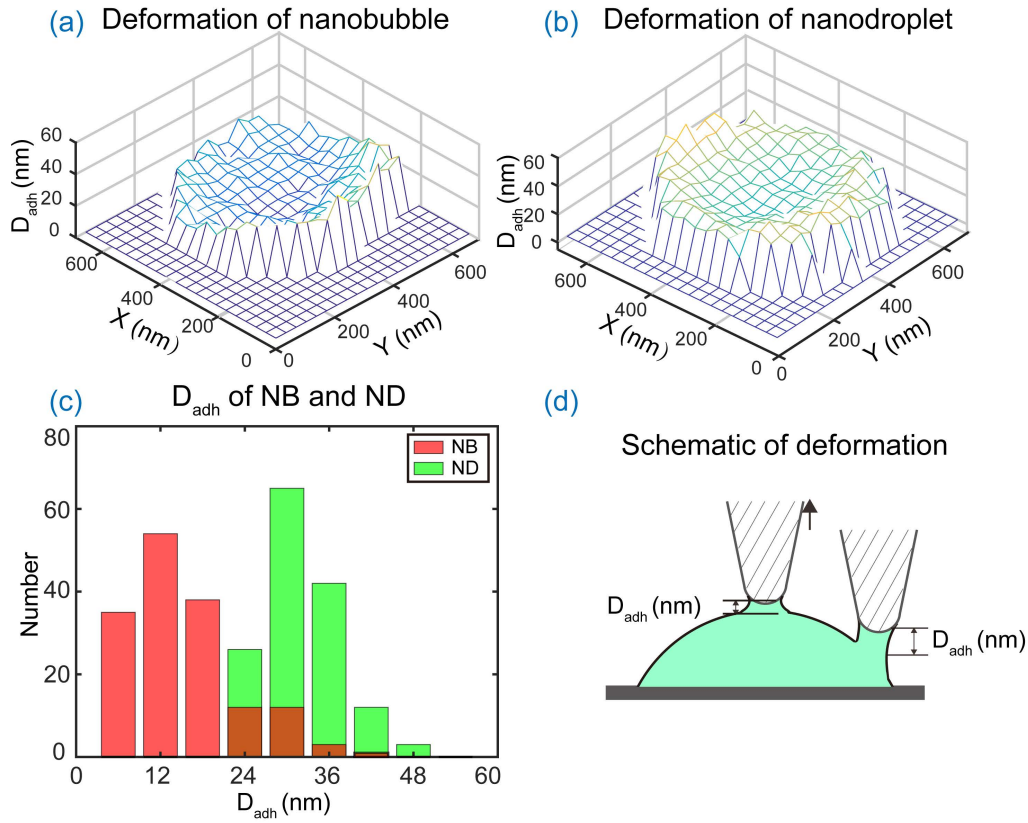
Figure 7: Comparison of deformation between the NB and the ND. The constructed maps of the deformation D_{adh} for the NB (a) and the ND (b). (c) The comparison of the histograms of D_{adh} on the NB and ND. (d) Schematic of the deformation of NB/ND by the AFM tip. Due to the higher viscosity value of PDMS than water, D_{adh} on the ND is much larger than that on the NB.

From the above results, one can see that the three nano-objects are distinguishable by using one approach or the combination of several approaches through morphological characterization and force spectroscopy measurement. The distinguishability of one object to the other two objects is summarized in table 2. One can see that blisters have the highest distinguishability among the three nano-objects. They can be distinguished from the other two kinds of nano-objects, no matter based on

15

CA measurement, high load scanning, or force spectroscopy measurement. The challenge remains on the distinction of NBs and NDs from each other. The major reason is that both NBs and NDs are all soft in nature and have either liquid/gas or liquid/liquid interfaces. As a result, they show similar response to high load scanning, exhibiting high mobility and deformability. Fortunately, they are distinguishable through volume measurement in coalescence experiment. NBs show significantly increased volume after coalescence, while the volume of NDs remains the same before and after coalescence. Regarding force spectroscopy measurement, NBs and NDs can be distinguished through quantitative evaluation, based on the fact that the surface tension value in the two cases is different.

Table 2: The distinguishability of the nano-objects.

	CA	Response to high load			Force spectroscopy		
		Mobility	Deformability	Volume	S_{def}	F_{adh}	D_{adh}
Nanobubble	✗	✗	✗	✓	✓	✓	✓
Nanodroplet	✗	✗	✗	✓	✓	✓	✓
Blister	✓	✓	✓	—	✓	✓	✓

Conclusion

In this study, the distinction among surface NBs, NDs and blisters was systematically investigated with an AFM through three approaches: morphological characterization, high load scanning, and force spectroscopy measurement. The results show that blisters can be easily distinguished from the other two nano-objects. They have the lowest contact angle values and are not movable and deformable under high scanning loads. The force spectroscopy measurement on the blisters is close to that obtained on solid surface.

The NBs and NDs have similar contact angles. They are all movable and deformable, and exhibit similar response at force-distance curves. However, they can be well distinguished by volume and

16

force spectroscopy measurement. The volume of NBs significantly increased after coalescence, while it remains the same for NDs. This is because of the reduced inner pressure and gas diffusion from liquid to the coalesced NBs. In the force spectroscopy measurement, three parameters, the prefactor S_{def} of linear tip-NB/ND interaction region, the adhesion force F_{adh}, and the deformation D_{adh} are extracted. The results show that NBs have larger S_{def}, F_{adh}, which agrees well with the fact that the water/air surface tension is higher than water/oil. On the contrary, D_{adh} on NBs is much smaller than that on NDs, due to the lower viscosity of water. We believe that this work provides a useful approach to identify NBs, NDs and blisters and is particularly useful in surface NB studies.

Supporting Information

Supporting Information File 1:

File Name: S1.pdf

File Format: PDF

Title: Supplementary materials

References

1. Mahnke, J.; Stearnes, J.; A. Hayes, R.; Fornasiero, D.; Ralston, J. *Phys. Chem. Chem. Phys.* **1999**, *1*, 2793–2798.

2. Wang, Y.; Bhushan, B. *Soft Matter* **2009**, *6*, 29–66.

3. Li, D.; Wang, Y.; Pan, Y.; Zhao, X. *Applied Physics Letters* **2016**, *109*, 237–240.

4. Wang, Y.; Zeng, B.; Alem, H. T.; Zhang, Z.; Charlaix, E.; Maali, A. *Langmuir* **2018**, *34*, 1371–1375.

5. Liu, S.; Duvigneau, J.; Vancso, G. J. *Eur. Polym. J.* **2015**, *65*, 33 –45.

6. Gao, L.; Ni, G.-X.; Liu, Y.; Liu, B.; Castro Neto, A. H.; Loh, K. P. *Nature* **2014**, *505*, 190–194.

7. Su, Y.; Ji, B.; Zhang, K.; Gao, H.; Huang, Y.; Hwang, K. *Langmuir* **2010**, *26*, 4984–4989.

8. Wang, Y.; Bhushan, B.; Zhao, X. *Nanotechnology* **2009**, *20*, 045301.

9. Zakzeski, J.; Bruijnincx, P. C. A.; Jongerius, A. L.; Weckhuysen, B. M. *Chem. Reviews* **2010**, *110*, 3552–3599.

10. Luo, J.; Im, J.-H.; Mayer, M. T.; Schreier, M.; Nazeeruddin, M. K.; Park, N.-G.; Tilley, S. D.; Fan, H. J.; Grätzel, M. *Science* **2014**, *345*, 1593–1596.

11. Wang, Y.; Li, X.; Ren, S.; Tedros, A. H.; Yang, L.; Lohse, D. *Soft Matter* **2017**, *13*, 5381–5388.

12. Carambassis, A.; Jonker, L. C.; Attard, P.; Rutland, M. W. *Phys. Rev. Lett.* **1998**, *80*, 5357–5360.

13. Tyrrell, J. W. G.; Attard, P. *Phys. Rev. Lett.* **2001**, *87*, 176104.

18

351 14. Jensen, T. R.; Jensen, M. O.; Reitzel, N.; Balashev, K.; Peters, G. H.; Kjaer, K.; Bjornholm, T.

352   *Phys. Rev. lett.* **2003**, *90*, 086101.

353 15. Mezger, M.; Reichert, H.; Schoeder, S.; Okasinski, J.; Schroeder, H.; Dosch, H.; Palms, D.;

354   Ralston, J.; Honkimaki, V. *Proc. Nat. Acad. Sci.* **2006**, *103*, 18401–18404.

355 16. Zhang, X. H.; Khan, A.; Ducker, W. A. *Phys. Rev. Lett.* **2007**, *98*, 136101.

356 17. Zhang, X. H.; Quinn, A.; Ducker, W. A. *Langmuir* **2008**, *24*, 4756–4764.

357 18. Chan, C. C.; Ohl, C.-D. *Phys. Rev. Lett.* **2012**, *109*, 174501.

358 19. Karpitschka, S.; Dietrich, E.; Seddon, J. R. T.; Zandvliet, H. J. W.; Lohse, D.; Riegler, H.

359   *Phys. Rev. Lett.* **2012**, *109*, 066102.

360 20. Zhang, X.; Lhuissier, H.; Sun, C.; Lohse, D. *Phys. Rev. Lett.* **2014**, *112*, 144503.

361 21. Borkent, B. M.; Dammer, S. M.; Schönherr, H.; Vancso, G. J.; Lohse, D. *Phys. Rev. Lett.*

362   **2007**, *98*, 204502.

363 22. Berkelaar, R. P.; Dietrich, E.; Kip, G. A. M.; Kooij, E. S.; Zandvliet, H. J. W.; Lohse, D. *Soft*

364   *Matter* **2014**, *10*, 4947–4955.

365 23. Berkelaar, R. P.; Bampoulis, P.; Dietrich, E.; Jansen, H. P.; Zhang, X.; Kooij, E. S.; Lohse, D.;

366   Zandvliet, H. J. W. *Langmuir* **2015**, *31*, 1017–1025.

367 24. Bonaccurso, E.; Butt, H.; Franz, V.; Graf, K.; Kappl, M.; Loi, S.; Niesenhaus, B.; Chem-

368   nitz, S.; Bohm, M.; Petrova, B.; Jonas, U.; Spiess, H. *Langmuir* **2002**, *18*, 8056–8061.

369 25. Xu, L.; Sharma, A.; Joo, S. W. *Macromolecules* **2012**, *45*, 6628–6633.

370 26. Li, D.; Liu, Y.; Qi, L.; Gu, J.; Tang, Q.; Wang, X.; Bhushan, B. *Langmuir* **2019**, *35*,

371   3005–3012.

372 27. Zhang, X. H.; Li, G.; Maeda, N.; Hu, J. *Langmuir* **2006**, *22*, 9238–9243.

19

28. Weijs, J. H.; Seddon, J. R. T.; Lohse, D. *Chem. Phys. Chem.* **2012**, *13*, 2197–2204.

29. Chan, C. U.; Chen, L.; Arora, M.; Ohl, C.-D. *Phys. Rev. Lett.* **2015**, *114*, 114505.

30. Seo, D.; German, S. R.; Mega, T. L.; Ducker, W. A. *J. Phys. Chem. C* **2015**, *119*, 14262–14266.

31. An, H.; Tan, B. H.; Ohl, C.-D. *Langmuir* **2016**, *32*, 12710–12715.

32. Wang, X.; Zhao, B.; Hu, J.; Wang, S.; Tai, R.; Gao, X.; Zhang, L. *Phys. Chem. Chem. Phys.* **2016**, *19*, 1108.

33. Reiter, G. *Langmuir* **1993**, *9*, 1344–1351.

34. Lohse, D.; Zhang, X. *Rev. Mod. Phys.* **2015**, *87*, 981–1035.

35. An, H.; Liu, G.; Craig, V. S. *Advances in Colloid and Interface Science* **2014**, *222*, 9–17.

36. Wang, Y.; Zhang, Z.; Wang, H.; Bi, S. *Plos One* **2015**, *10*, e0130178.

37. Wang, Y.; Lu, T.; Li, X.; Wang, H. *Beilstein J. Nanotech.* **2018**, *9*, 975–985.

38. Wang, Y.; Wang, H.; Bi, S.; Guo, B. *Beilstein J. Nanotech.* **2015**, *6*, 952–963.

39. Wang, Y.; Lu, T.; Li, X.; Ren, S.; Bi, S. *Beilstein J. Nanotech.* **2017**, *8*, 2572–2582.

40. Wang, Y.; Bhushan, B.; Zhao, X. *Langmuir* **2009**, *25*, 9328–9336.

41. Yang, S.; Kooij, E. S.; Poelsema, B.; Lohse, D.; Zandvliet, H. J. W. *EPL* **2008**, *81*, 64006.

42. Heslot, F.; Fraysse, N.; Cazabat, A. M. *Nature* **1989**, *338*, 640–642.

43. An, H.; Liu, G.; Atkin, R.; Craig, V. S. J. *ACS Nano* **2015**, *9*, 7596–7607.

44. Zhang, X. H.; Maeda, N.; Craig, V. S. J. *Langmuir* **2006**, *22*, 5025–5035.

45. Wang, Y.; Wang, H.; Bi, S.; Guo, B. *Sci Rep* **2016**, *6*, 30021.

393 46. Walczyk, W.; Schönherr, H. *Langmuir* **2014**, *30*, 11955–11965.

394 47. Guo, Z.; Liu, Y.; Xiao, Q.; Schoenherr, H.; Zhang, X. *Langmuir* **2016**, *32*, 751–758.